Journal of Thermal Analysis and Calorimetry (2023) 148:7747–7765
https://doi.org/10.1007/s10973-023-12277-z

Oxygen production at intermediate temperatures using $Ca_2AlMnO_{5+\delta}$ double perovskite-type oxides

Mehdi Pishahang[1,2] · Yngve Larring[1] · Schalk Cloete[1] · Martin Fleissner Sunding[1] · Christelle Denonville[1] · Zuoan Li[1]

Received: 24 November 2022 / Accepted: 18 May 2023 / Published online: 13 June 2023

Abstract

Double-perovskite $Ca_2AlMnO_{5+\delta}$ exhibits promising oxygen uptake and release capacity at intermediate temperatures (400–700 °C), which makes it an interesting candidate for in situ oxygen production in an integrated gasification combined cycle (IGCC) process. Experiments were conducted at 10 bars by alternating gas feeds of air and various sweep gases to a packed bed filled with 300 g of granular oxygen carrier materials. These realistic operating conditions demonstrated that 15–20% oxygen can be introduced to the sweep gas, which is sufficient for autothermal gasification of solid fuels in IGCC. Argon performed slightly better than CO_2 as a sweep gas, presumably because of some CO_2 absorption or the higher O_2 partial pressure of CO_2 that inhibited O_2 release. Further O_2 concentration increases can be expected from increasing the temperature under reduction by feeding a fuel gas to combust with the released O_2, but experiments with H_2 did not produce the desired effect because the combustion reaction was too slow at the optimal reactor temperature (~600 °C). In general, the reduction stage was more prone to kinetic limitations, as illustrated by a significant decrease in O_2 concentration when the sweep flowrate was increased. A longer oxidation stage to fully charge the oxygen carrier also increased O_2 concentrations in the sweep, but this requires a process integration such as IGCC where the large quantity of warm depleted air can be effectively utilized. Furthermore, the enthalpy of oxidation of $Ca_2AlMnO_{5+\delta}$ was obtained from density functional theory modeling, equilibrium conditions in thermogravimetric analysis, packed bed experiments and directly from differential scanning calorimetry. The enthalpy of oxidation obtained by these techniques range from – 166 to – 196 kJ mol^{-1} O_2.

Keywords Chemical looping combustion · Fixed bed reactor · Oxygen carrier material · Calcium aluminate manganate · Syngas

Abbreviations

BPC	Back pressure controller
EDS	Energy-dispersive X-ray spectroscopy
IGCC	Integrated gasification combined cycle
CAM	$Ca_2AlMnO_{5+\delta}$
CASU	Cryogenic air separation unit
CLAS	Chemical looping air separation
CLC	Chemical looping combustion
CL-IGCC	Chemical looping integrated gasification combined cycle
CLOP	Chemical looping oxygen production
DFT	Density functional theory
DSC	Differential scanning calorimetry
GGA	Generalized gradient approximation
MFC	Mass flow controller
OCM	Oxygen carrier material
PBCLC	Packed bed chemical looping combustion
PSA	Pressure swing adsorption
SEM	Scanning electron microscopy
TGA	Thermogravimetric analysis
TSA	Temperature swing adsorption
XPS	X-ray photoelectron spectroscopy

✉ Yngve Larring
Yngve.Larring@SINTEF.no

Mehdi Pishahang
Mehdip@MIT.edu

[1] SINTEF Industry, Sustainable Energy Technologies, P.O. Box 124, NO-0314 Blindern, Oslo, Norway

[2] Department of Mechanical Engineering, Massachusetts Institute of Technology, 77 Massachusetts Avenue, Cambridge, MA, USA

Introduction

The goal of the Paris Agreement is to mitigate climate change by limiting the rise in global temperature to well below 2 °C by the year 2100 [1]. A portfolio of technologies capable of reducing CO_2 emissions at large scale is needed to achieve this goal. CO_2 capture and storage (CCS) is one of these technologies. In the 2 °C scenario (2DS) of the International Energy Agency (IEA), CCS technologies will contribute 14% of the cumulative CO_2 emissions reduction from 2020 to 2060, amounting to 142 $GtCO_2$ [2]. In comparison, the capacity of the 23 large-scale CCS projects currently in operation and under construction is about 0.04 $GtCO_2$/year [3]. A massive large-scale deployment of CCS technologies is required to fill this large gap.

Several new technologies based on chemical looping systems have shown superior techno-economics compared to postcombustion capture in terms of CO_2 avoidance cost [4, 5]. Concepts based on oxyfuel combustion with an oxidant stream supplied by Chemical Looping Air Separation (CLAS), also known as chemical looping oxygen production (CLOP), can achieve 75–80% lower oxygen production energy demand than a conventional cryogenic air separation unit (CASU). The promise of these technologies is heavily dependent on the development of suitable materials, which is the focus of the present study. Further details on the targeted process and the material are provided in the subsequent sections.

Chemical looping oxygen production (CLOP) process

Chemical looping oxygen production (CLOP) is a promising technology for air separation with a considerably lower energy penalty than conventional CASU [6]. As a standalone system, such a plant requires large recuperative heat exchangers to pre-heat incoming air with outgoing depleted air and to recover steam condensation enthalpy for undiluted steam generation, which will be used as sweep gas. Additional energy input is required to maintain the system heat at the correct reaction temperature during the endothermic oxygen release (reduction of oxygen carrier material).

One method for avoiding these complexities is the integration of the CLOP system into a chemical looping integrated gasification combined cycle (CL-IGCC) plant (Fig. 1) [6]. This plant configuration uses the heated depleted air stream from the CLOP oxidation step directly in the CLC reactors to be further heated for driving a power cycle. The sweep gas in the reduction step is a mixture of cleaned syngas and combustion products from the CLC reactors, thus avoiding the need to generate additional steam for use as sweep gas. The fuel gases in the sweep gas react with the released oxygen to provide the heat for the endothermic reduction reaction and maintain the reactor temperature at the required level.

This plant configuration can improve power plant efficiency relative to a IGCC plant using only chemical looping combustion (CLC) with CASU by 2.3% points [7], which is more than half of the energy penalty imposed by the CASU. The main challenge with this approach is the low oxygen concentration (12–18%) in the CLOP reduction step outlet gas, which will be fed into the gasifier. This increases the

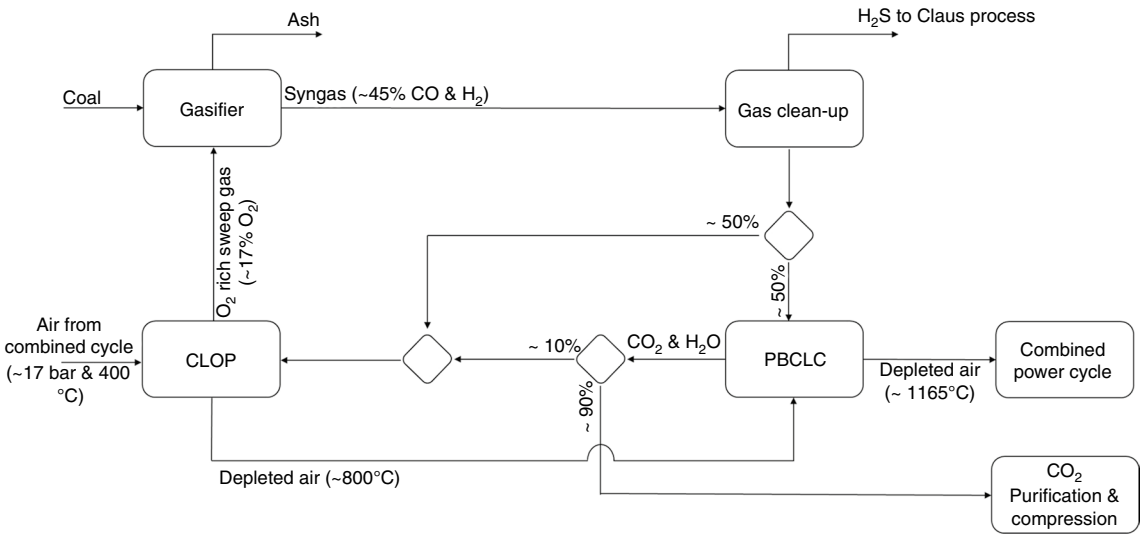

Fig. 1 Schematic of the integration of CLOP into a CLC-IGCC plant [6]

cost of the gasifier and the gas cleanup unit, eroding most of the economic benefits from the efficiency gain [6]. Two potential solutions that can be explored in future work are 1) the use of a pressure swing in the CLOP reactors, operating the reduction step at a lower absolute pressure to increase the mole fraction of O_2 in the reduction step outlet gases, or 2) a temperature swing, which can increase the oxygen release drastically as we demonstrate in this work. Optimization of the oxygen production is of high importance for reducing the size/cost of gasifier (typically the most expensive unit in IGCC power plants) and increasing the heating value of the syngas produced in the gasifier, which would reduce the size and increase efficiency of the downstream process units.

$Ca_2AlMnO_{5+\delta}$ double-perovskite material

Perovskite-type oxides with the general formula of $ABO_{3-\delta}$ (where *A* is normally an alkaline-earth or rare-earth metal, and *B* is normally a transition metal) have attracted great interest as promising oxygen carrier materials (OCMs) to overcome the phase transformation issues observed in the binary transition metal oxides. The ideal perovskite has a cubic structure, where the *B* cations occupy the octahedral sites in the closed pack cubic AO_3 framework. As an alternative, the perovskite structure can be seen as a cube with an *A* cation in the center and *B* cations on BO_6 octahedrons on the edges [8]. The *A* cation is coordinated with 12 oxygen atoms.

In terms of redox performance, perovskites possess an important advantage over most binary transition metal oxides, due to variable oxygen non-stoichiometry. Since the first-row transition metals in the periodic table normally have more than one oxidation state, oxygen non-stoichiometry in the perovskite oxides with such metals on the *B*-site has often been observed [9]. In addition, their re-oxidation is often reversible because the reduced phase is still a stable oxide structure, so they can undergo many redox cycles without structural deterioration. A double-perovskite structure is formed when exactly half of *B*-site cations is replaced by another *B*' cation, and a rock salt ordering between these two is achieved [10]. Double perovskite has begun a new era for perovskites, since the ordering in double-perovskite structures often enable redox activity at lower temperatures than regular perovskites. The material of focus in our study is CAM ($Ca_2AlMnO_{5+\delta}$), a double perovskite with Ca in the *A* site and ordered Al and Mn layers in the *B* site [10–13]. CAM consists of cheap and abundant elements with minimal environmental and health issues, while possessing a large oxygen uptake-release capacity at intermediate temperatures (400–700 °C) [13–17]. CAM and other double perovskites have been studied for high-temperature pressure swing adsorption (PSA) [18–20], even though pressurization and depressurization of the gas is energetically costly, which deems the PSA approach suboptimal. But these characteristics qualify CAM as a promising candidate for large-scale operation and integration into an IGCC process, where it will be used to create oxygen at intermediate temperatures, driven by a combined temperature and partial pressure swing. The correct temperature swing will also overcome the hysteresis effect more efficiently.

CAM-based [11–19, 21–24] and other double-perovskite materials [25–27] have recently received a lot of attention for their high oxygen mobility at comparatively low temperatures of 400–700 °C. What makes CAM special is that, although Al in the *B* site remains always 3+ valence and it is Mn in the *B* site that oxidizes from 3+ to 4+, the absorbed oxygen anions are collected in the Al sub-layer [11, 13]. The oxidation enthalpy involved in this reaction was reported to be 185.6, 143.5, 143.6, 139.8 kJ mol^{-1} for $Ca_{1-x}Sr_xAlMnO_5$ with $x = 0$, 0.5, 0.8, 1, respectively [19]. Tian et al. [17] reported an oxidation enthalpy and entropy of 146.5 kJ mol^{-1} O_2 and 162.7 J K^{-1} mol^{-1} O_2 based on the van't Hoff approach. The same paper reports oxidation enthalpy and entropy of 136.9 kJ mol^{-1} O_2 and 225.3 J K^{-1} mol^{-1} O_2 based on the defect chemistry models. A similar defect chemistry approach used by Ling et al. resulted in an oxidation enthalpy of 160.8 kJ mol^{-1} O_2 [22], while Tanahashi et al. reported a mean enthalpy of oxidation of 191 kJ mol^{-1} O_2 obtained from a packed bed experiment [18].

As shown in Fig. 2, the Mn sub-layer in both reduced and oxidized forms of the oxide is always fully loaded with oxygen and the additional oxygens in the oxidized material are indeed added to the Al sub-layer. This redox decoupling due to ordering is unprecedented and enables a new method of modifying the redox performance of an oxide, beyond simple doping. Doping attempts to improve reversibility [19, 22, 24] have shown that some improvement can be made. However, the primary findings were that the oxygen release temperature can be manipulated and that, in some cases (Sr-doped) [19, 24], the kinetics can also be enhanced with lowered oxidation enthalpy, resulting in lower energy demand for oxygen production by PSA.

To date, the main application for CAM has been found in electrodes for low temperature ceramic electrolyzers and fuel cells, as well as oxygen production [17–19, 23, 27]. Motohashi *et.al* [14] investigated the effect of phase purity and non-stoichiometry on the performance sensitivity. Their paper also demonstrates excellent redox characteristics of this material at intermediate temperatures. Motohashi's second publication [16] shows that CAM exhibits a nearly 100 °C hysteresis effect on oxidation and reduction between the oxygen uptake and release steps (according to Eqs. 1 and 2).

$$Ca_2AlMnO_{5+\delta} \rightarrow Ca_2AlMnO_5 + \delta/2\ O_2(\text{to steam}) \quad (1)$$

$$Ca_2AlMnO_5 + \delta/2\ O_2(\text{from air}) \rightarrow Ca_2AlMnO_{5+\delta} \quad (2)$$

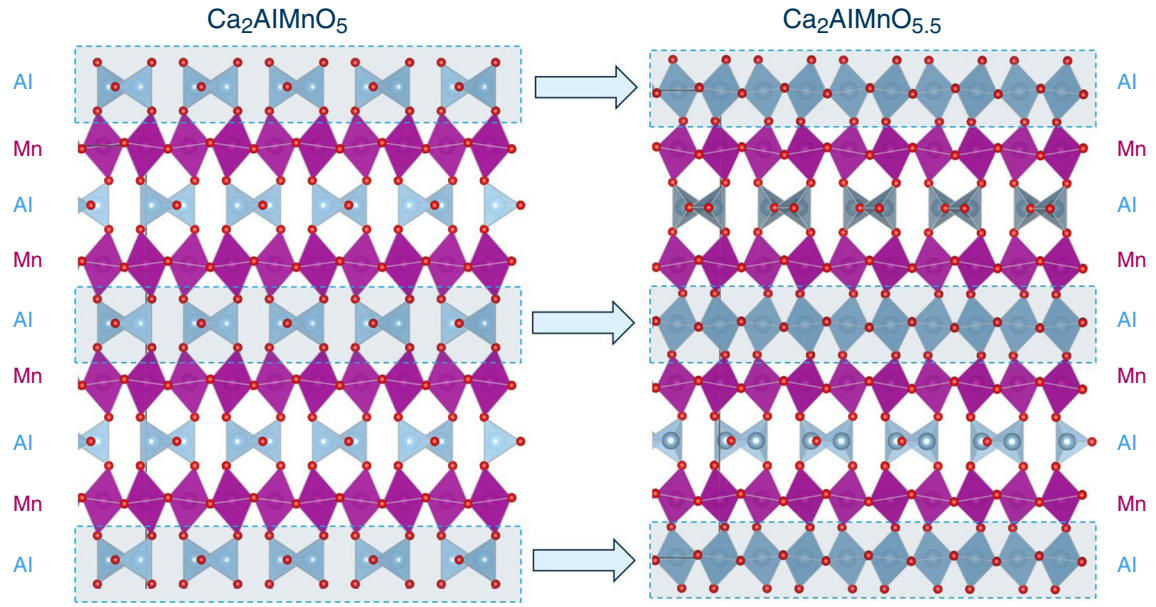

Fig. 2 Structure of the reduced and oxidized $Ca_2AlMnO_{5+\delta}$ (CAM) material. The experimental structures for the reduced and oxidized phases are extracted from the following references: Ca_2AlMO_5 [28] and $Ca_2AlMO_{5.5}$ [12]

This work investigates the redox thermodynamics of Mn^{3+} to Mn^{4+} in CAM through experimental and quantum modeling approaches. Its cationic valent stability and oxygen binding energies are studied both by DFT and XPS and compared to oxidation of Mn^{3+} to Mn^{4+} energetics in other oxides. This comparison allows us to understand the important role played by the ordered layered structure in CAM to facilitate oxygen ion mobility and therefore the redox characteristics of the material. Thermogravimetric analysis (TGA) has been used to understand the oxygen uptake and release reversibility and kinetics. The optimization of the synthesis and extrusion fabrication allowed us to manufacture a kilogram batch for testing only 300 g was used in the packed bed CLOP reactor, by which we investigated the important parameters influencing oxygen production in a more relevant gas to solid ratio than TGA. As the enthalpy of oxidation of CAM is non-negligible in such a setting, the packed bed reactor allows for a more realistic simulation of non-isothermal redox conditions, as well as other process-related parameters such as time of oxidation/reduction, gas speed and temperature range. In this study, we use an in-house temperature swing adsorption (TSA) packed bed reactor (using roughly 300 g granular oxygen carrier materials) to study the CLOP performance of the CAM material under realistic conditions.

Experimental procedure

Quantum modeling

In this work, we use quantum modeling to obtain the enthalpy of oxidation of $Ca_2AlMnO_{5+\delta}$. By comparing the formation energies of the reactants and products of Eq. 3, we can obtain the oxidation enthalpy of Mn^{3+} to Mn^{4+} in CAM. In order to reproduce the layered structures, $5 \times 1 \times 5$ supercells consisting of 16 Ca ions were constructed. The initial structures for both Ca_2AlMO_5 [28] and $Ca_2AlMO_{5.5}$ [12] are experimentally reported structures extracted from The Materials Project [29]. These initial structures (Fig. 2) are relaxed in all 3 dimensions and volume until a fully relaxed structure was achieved. The total energies of the calcium, aluminum and manganese oxides were calculated with the generalized gradient approximation (GGA) to DFT and with the GGA + U extension, with Perdew–Burke–Ernzehof (PBE) functionals [30, 31]. Projector augmented-wave (PAW) [32, 33] pseudopotentials implemented in VIENNA AB INITIO SIMULATION PACKAGE (VASP 5.3.2) [34] was used. In order to reach converged energies within 0.2 mV per

formula unit, an energy cutoff of 500 eV and large Monkhorst–Pack grids of $11 \times 2 \times 11$ were chosen. The tetrahedron method with Blöch corrections was used for smearing, which is known to produce the total energies more accurately. J and U values of $J = 0.98$ and $U = 4.0$ eV were used, which are known to predict the Mn oxide systems with different Mn valent states [35]. In all calculations, atom coordinates, lattice vectors and cell volumes were fully relaxed for each structure to obtain all forces smaller than 1 mRy/a.u. Given the importance of the correct magnetic structure and its influence on the total energies [36], spin polarization was deployed in the calculations with the experimentally reported G-type antiferromagnetic structure and Mn magnetic moments of 4 μ_B, which corresponds to the Hund's prediction for Mn. The total energy of oxygen is calculated through relaxation of a triplet O_2 molecule in a cubic box with edge length of 10 Å, starting with the experimental O–O distance of 121 pm [37].

For a spin-polarized O_2 molecule, the calculated equilibrium bond length is 122 pm, the total energy per molecule is 10.03 eV/O_2, while the corresponding dissociation energy is 6.31 eV/O_2. Although these values are in good agreement with the previous GGA reports, the dissociation energy is more than 1 eV/O_2 higher than the experimental value. This O_2 overbinding is a known systematic error, which can easily be corrected for by applying Wang's fixed ad hoc correction parameter of 131 kJ mol^{-1} O_2 [35].

Table 1 Volumetric composition of the prepared and used CAM paste

Component	Paste volumetric content/vol%
Ceramic/dry extrudate	57
Pore formers/dry extrudate	34
Binders/ceramic ratio	4

$$4Ca_2AlMnO_5 + O_2 \rightarrow 4\,Ca_2AlMnO_{5.5} \quad (3)$$

Material synthesis, fabrication and characterization

$Ca_2AlMnO_{5+\delta}$ (CAM) powder was purchased from CERPOTECH AS (Norway), which synthesized the powder by spray pyrolysis. The particle size distribution was characterized using image analysis on dry powder (Malvern Morphology G3). To prepare porous granulates, the CAM powder was firstly mixed with two pyrolyzable fillers, corn starch (Carl Roth) and charcoal (Merck) in a 1:1 volume ratio, followed by addition of a proprietary water soluble binder system and a polyglycol plasticizer (see Table 1). The mixing was carried out until a homogeneous paste was obtained.

The paste was extruded as rods of 3 mm in diameter using a capillary extruder at a pressure of 3.6 atm. The rods were dried at room temperature and cut into smaller segments of approximately 2–4 cm long (Fig. 3). In order to obtain mechanically strong and porous granulates, several annealing schedules were investigated with temperature ranging from 900 to 1350 °C, and sintering time ranging from 2 to 12 h. The protocol selected to obtain a porosity of about 30 vol% in the granulates is as follows. The dried segments were firstly sintered in air at 1250 °C for 12 h with both heating and cooling rates of 100 °C h^{-1}, followed by a second annealing in flowing nitrogen at 1250 °C for 12 h with both heating and cooling rates of 120 °C h^{-1}. This method enabled to produce batches of about 120 g of rods after sintering.

The porosity of the granulates was calculated from geometrical dimensions and Archimedes' method. The structure of the material was analyzed by X-ray diffraction using a PANalytical Empyrean diffractometer with Cu Kα radiation and PIXcel^{3D} detector, while the microstructure was observed by microscopy using field emission gun (FEG) scanning electron microscopy (SEM) using a FEI Nova NanoSEM 650 apparatus with energy-dispersive X-ray

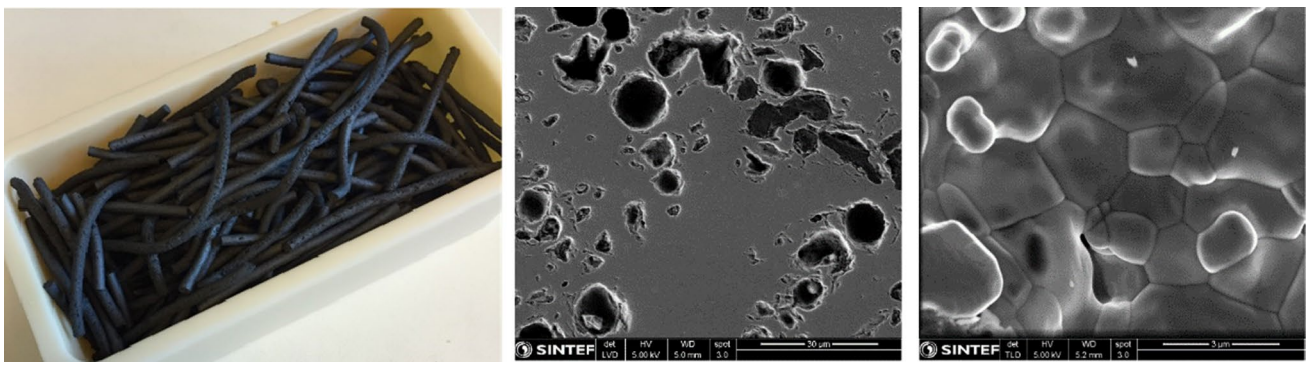

Fig. 3 Left: extruded and sintered CAM used in the packed bed reactor testing. Middle and right: cross-section views of sintered granulates with various magnifications after polishing of sample embedded in resin (middle) and fresh surface (right)

spectroscopy (EDS). X-ray photoelectron spectroscopy (XPS) was performed on a Kratos Axis Ultra^{DLD} instrument for the characterization of the chemical state of the elements in the material in the reduced and oxidized states. Monochromatic Al Kα radiation was used for the measurements, and the energy scale was calibrated based on the position of the C 1s peak related to the aliphatic bonds of adventitious carbon, set to 284.8 eV binding energy (BE).

The initial powder from CERPOTECH AS has a mean size diameter of 2.5 µm with more than 70% in the range of 1–10 µm. After sintering, the granulates have a porosity of 32%, consisting of both closed pores and interconnected pores, as shown in Fig. 3. The granulates have grain sizes ranging from 1 to 3 µm (Fig. 3).

Thermogravimetry and calorimetry

A SETSys Evolution (SETARAM) thermogravimetric analyzer (TGA) apparatus coupled with a fully automated in-house gas mixing system was used. Regardless of the gas composition, a constant reactive gas total flow of 200 mL min^{-1} was used in all TGA experiments. An initial sample mass of 35 ± 5 mg was loaded in an alumina crucible. The sample underwent three sets of heat-up and cool-down sequences (up to 700 °C and down to 400 °C) in O_2 to charge and discharge the oxygen content prior to isothermal charge–discharge experiments. The incremental reduction and oxidation sequences were then performed from 400 to 600 °C with 20 °C increments between isotherms. Each reduction and oxidation step was repeated three times to make sure that the transient effects induced by the previous steps were removed. Each reduction and oxidation step was set for 30 min. O_2 was used as the oxidizing and N_2 as the

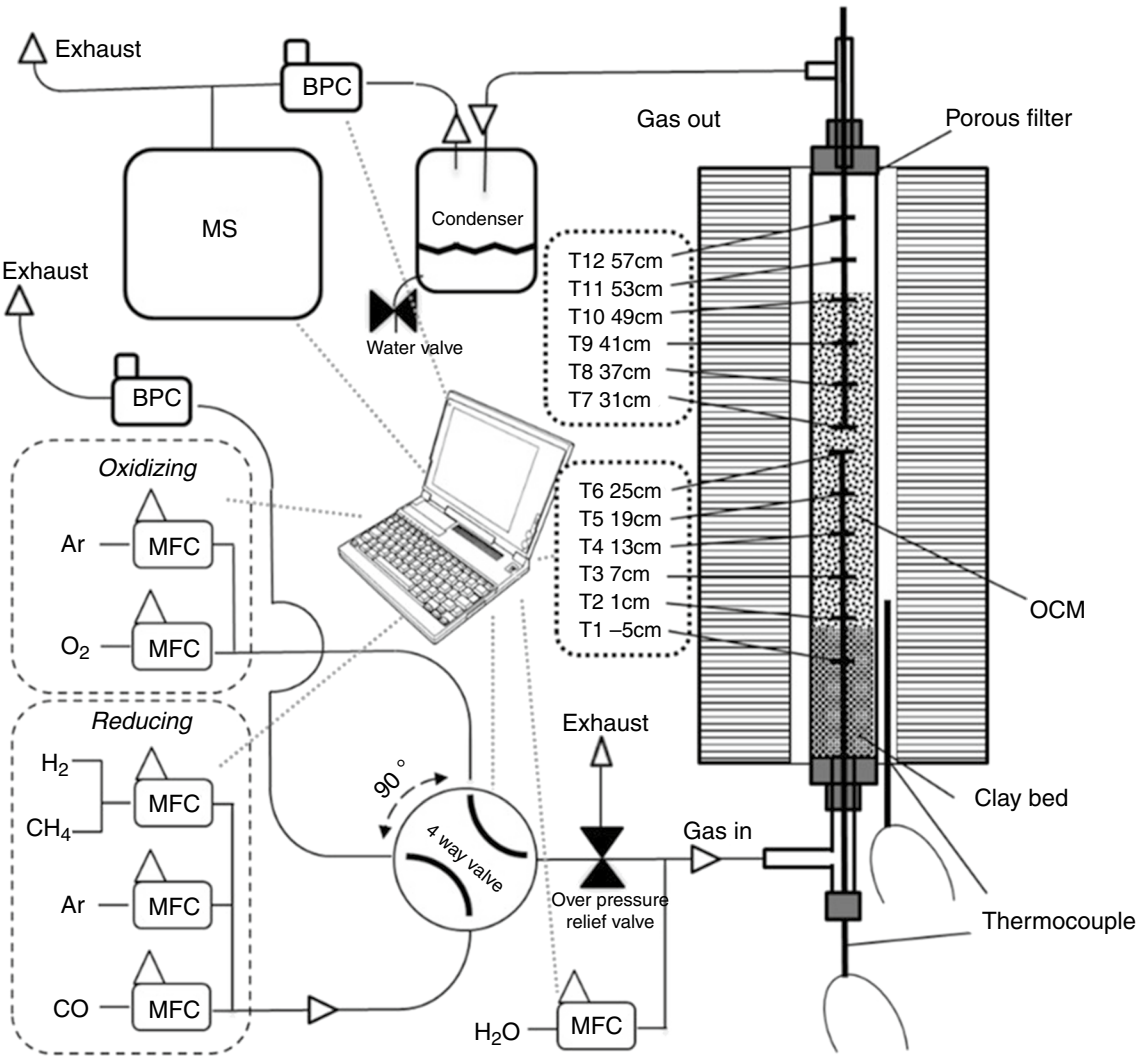

Fig. 4 Schematic illustration of the bench-top packed bed CLOP reactor used in this study and its components

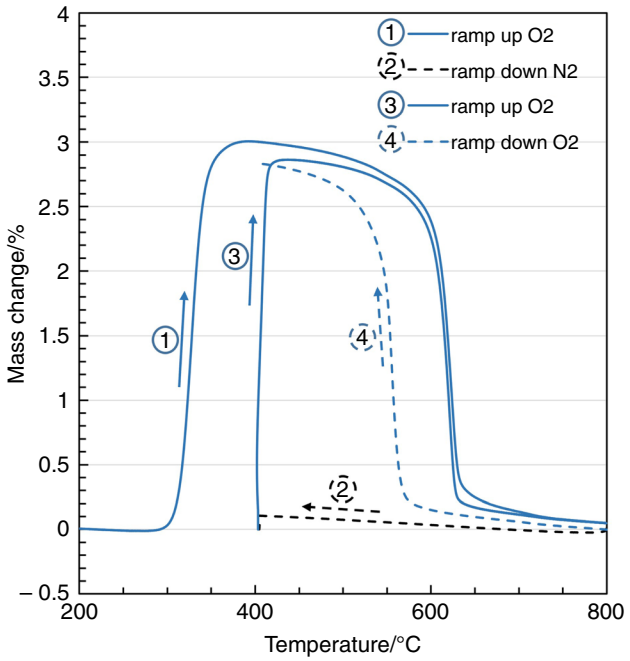

Fig. 5 Temperatures ramping up and down CAM in TGA in O_2 and N_2

reducing gas, while the total flow remained unchanged at 200 mL min^{-1}. These conditions were chosen to estimate the useful oxygen capacity and redox reaction rate, and to indicate the reversibility after each cycle. The buoyancy effect during TGA measurements is dependent on the molar mass of the gases used. Due to closer molar mass of N_2 to O_2, nitrogen (instead of Ar) was used as the reducing gas in all the experiments to minimize the effect of buoyancy imposed by different gas mixtures. The experiments were however repeated with an inert sample (alumina powder) to correct for the effect of buoyancy.

For the calorimetric experiments, a SETSYS Evolution TGA/DSC (SETARAM) was used. The device is calorimetrically calibrated by Sn (231.9 °C), Ag (961.8 °C) and Au (1064 °C), prior to the measurement to ensure accuracy, and as well to quantify the enthalpies of oxidation and heat capacity. Similar to the TGA experiments, the sample underwent three sets of heat up and cool down (to 700 °C and down to 400 °C) in O_2 to charge and discharge the oxygen content prior to the calorimetric experiment. The enthalpy of oxidation was then measured by increasing the temperature of the fully charged CAM in O_2 until the material is reduced under 1 atm O_2 pressure to remain in the thermodynamic standard condition.

Packed bed reactor experiments

The packed bed oxygen uptake and release experiments were conducted in a vertical fixed bed reactor at 10 atm, schematically presented in Fig. 4. This setup has been described in detail elsewhere [38]. The packed bed reactor consists of a boiler-grade stainless steel (Sandvik MA253 – Sweden) tube OD = 34.1 mm, ID = 26.5 mm and L = 800 mm), which is resistant to temperatures up to 1100 °C. A set of axial thermocouples, consisting of 6 K-type thermocouples (Skotselv–Norway) was inserted into the reactor from both sides, which allowed measuring the temperature at 12 positions along the reactor (60 mm between each). The reactor was positioned in a vertical tubular furnace (ID = 40 mm and L = 1000 mm), which was PID controlled separately by an external controller. A separate K-type thermocouple was used to measure the furnace temperature, and the thermocouple was placed well below the hot zone of the furnace.

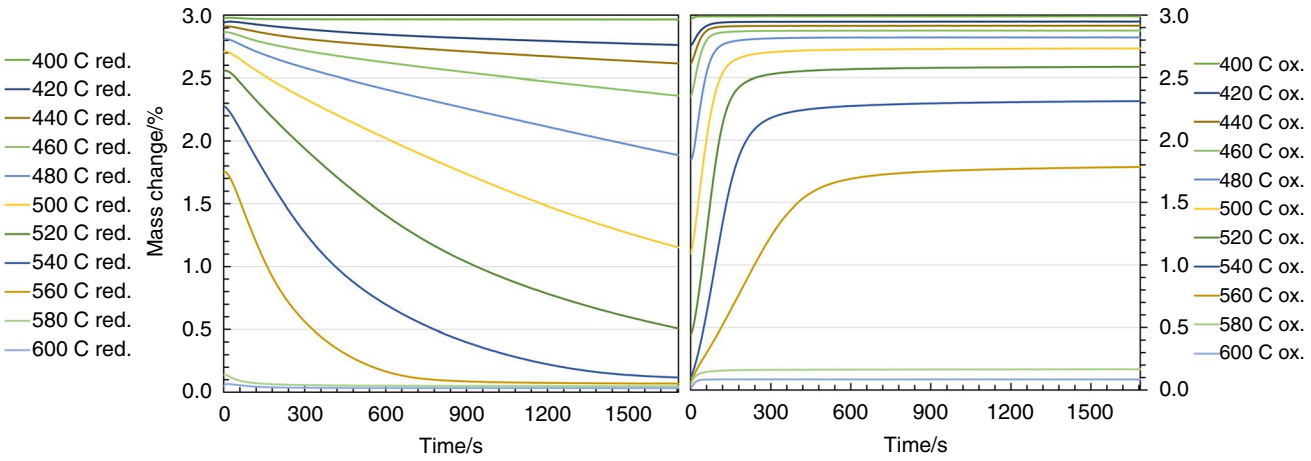

Fig. 6 The third redox cycle between O_2 and N_2 at different temperatures in a TG experiment running temperature ramps in O_2 and N_2 and then three isotherm redox cycles between O_2 and N_2 in the temperature range from 400 to 700 ℃. The first cycle shows a higher capacity than the next two reversible cycles

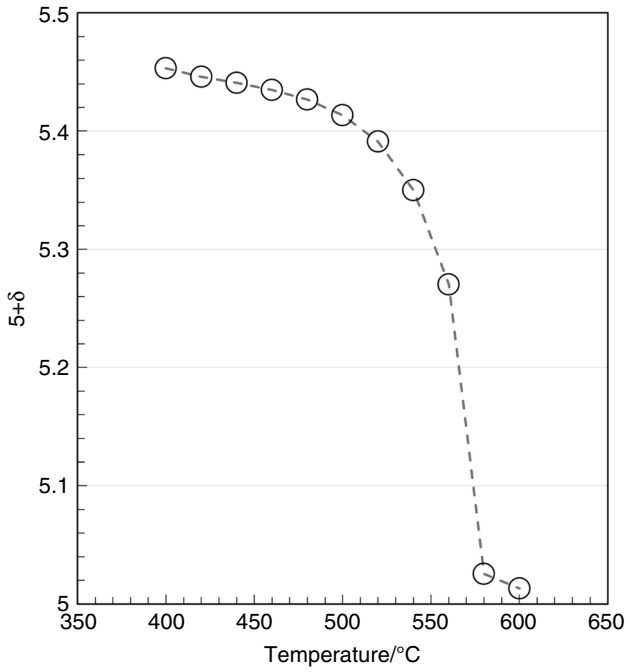

Fig. 7 Oxygen stoichiometry of CAM in pure oxygen (1 atm) as a function of temperature, extracted from isothermal TGA experiments

Thus, the thermocouple's temperature was not affected by the reactions happening in the reactor. As a result, the furnace temperature was kept constant during the experiment and therefore an invariable temperature profile across the upper section of the furnace where the OCM was set.

The oxygen carrier materials (OCMs) bed, 495 mm in height (300 g of CAM), was placed on top of the inert bed (110 mm) of alumina beads in the hot zone of the furnace with average bed porosity of ~ 60%. The OCM was in the form of cylindrical granulates with 32% porosity and had an average diameter and length of 2.5 mm and 20 mm, respectively. A high temperature filter was located above the OCM in order to avoid damaging sensitive down-stream equipment by the potential fines abraded from the granulates and carried on in the gas stream. A gas mixing system consisting of 6 mass flow controllers (MFCs) and two back pressure controllers (BPCs) was used to supply the reactive gas mixtures into the reactor and control the reactor's pressure. An automatic alternating 4-way valve (Valco) was used to switch between oxidizing and inert condition.

For safety reasons, a manual pressure relief valve was installed on the gas feed line with an opening pressure above 12 atm, in order to vent the entire feed gas to the exhaust in case the reactor or any of the outlet gas lines became clogged. The use of Ar as the reducing gas has two positive effects. The first is that, given the online gas analysis by MS, the inert reducing gas can be distinguished from N_2 which was fed together with O_2 during the oxidation as a component of air. The second benefit is the higher heat capacity of Ar compared to O_2 and N_2, thus the possibility of carrying more heat from the inline heater to the reactor during the reduction stage giving a TSA effect of up to 70 °C, thus a more pronounced temperature difference at the inlet between the oxidation and reduction steps. The feed and sweep gas to the reactor was preheated by an inline heater. An in-house LabView program was

Table 2 Enthalpies for oxidation of different materials using different models

$Mn^{3+} \rightarrow Mn^{4+}$ reaction systems	ΔH_{ox} kJ/mol O_2	Technique	References
$2Mn_2O_3 + O_2 = 2MnO_2$	− 175	Variety techniques	FactSage
$2/\delta Ca_2AlMnO_5 + O_2 = 2/\delta Ca_2AlMnO_{5+\delta}$	− 176	DSC	This study
$2/\delta Ca_2AlMnO_5 + O_2 = 2/\delta Ca_2AlMnO_{5+\delta}$	− 166	Gibbs (packed bed)	This study
$2/\delta Ca_2AlMnO_5 + O_2 = 2/\delta Ca_2AlMnO_{5+\delta}$	− 191	Gibbs (packed bed)	[18]
$2/\delta Ca_2AlMnO_5 + O_2 = 2/\delta Ca_2AlMnO_{5+\delta}$	− 185	van't Hoff (TGA)	This study
$2/\delta Ca_2AlMnO_5 + O_2 = 2/\delta Ca_2AlMnO_{5+\delta}$	− 146	van't Hoff (TGA)	[17]
$2/\delta Ca_2AlMnO_5 + O_2 = 2/\delta Ca_2AlMnO_{5+\delta}$	− 186	van't Hoff (TGA)	[19]
$4Ca_2AlMnO_5 + O_2 = 4Ca_2AlMnO_{5.5}$	− 137	DFT	[17]
$4Ca_2AlMnO_5 + O_2 = 4Ca_2AlMnO_{5.5}$	− 161	DFT	[22]
$4Ca_2AlMnO_5 + O_2 = 4Ca_2AlMnO_{5.5}$	− 196	DFT	This study

Table 3 Cation oxidation states in $Ca_2AlMnO_{5+\delta}$ system

Technique		Ion valence Ca_2AlMnO_5			Ion valence $Ca_2AlMnO_{5.5}$		
		Ca	Al	Mn	Ca	Al	Mn
Nominal		2+	3+	3+	2+	3+	4+
Bond-valence (Modeled by Brese & O'Keeffe)		1.95	2.85	3.25	2.16	2.91	3.87
XPS	$2p_{3/2}$ peak shape			3.0			3.5
XPS	3*s* peak separation			3.4			4.3

used to control the experiment and record the data from the mass flow controllers and back pressure controllers, as well as logging the temperatures, pressures and the mass spectrometer data. A mass spectrometer (Pfeiffer) was used to analyze the outlet gas of the reactor. The mass spectrometer was calibrated prior to experiments with corresponding gas mixtures. The reactor assembly and its components used in this study are illustrated in Fig. 4.

Results and discussion

Thermogravimetric analysis

Heating the reduced phase of CAM in a TGA in O_2 at 1 atmosphere shows that the sample oxidizes before 350 °C, see Fig. 5. The sample subsequently releases the uptaken oxygen when the temperature increases to 600 ℃ and is fully reduced again to the initial phase before 630 °C. Cooling the material in inert N_2 down to 400 °C and then adding pure O_2 gives a fast oxidation back to the oxidized structure, with an oxygen capacity of around 3mass%, as shown in Fig. 5. Note that if the material is fully reduced, reoxidation may not be fully reversible, and the full discharge may cause major loss of oxygen transfer capacity. It is therefore paramount not to fully reduce the material, and instead limit the discharge somewhat to ensure full reversibility. This behavior might be related to the stability of the reduced phase or hysteresis restrictions. Figure 5 demonstrates that 580–610 ℃ in the gas phase may be optimal temperatures for oxygen production. It is worth noting that CAM can also be used for thermochemical energy storage in air. The material essentially acts as a thermal buffer. If the inlet gas temperature decreases to below 400 °C, it will oxidize, and the exothermic nature of the oxidation increases the temperature to 500 °C (until the material's

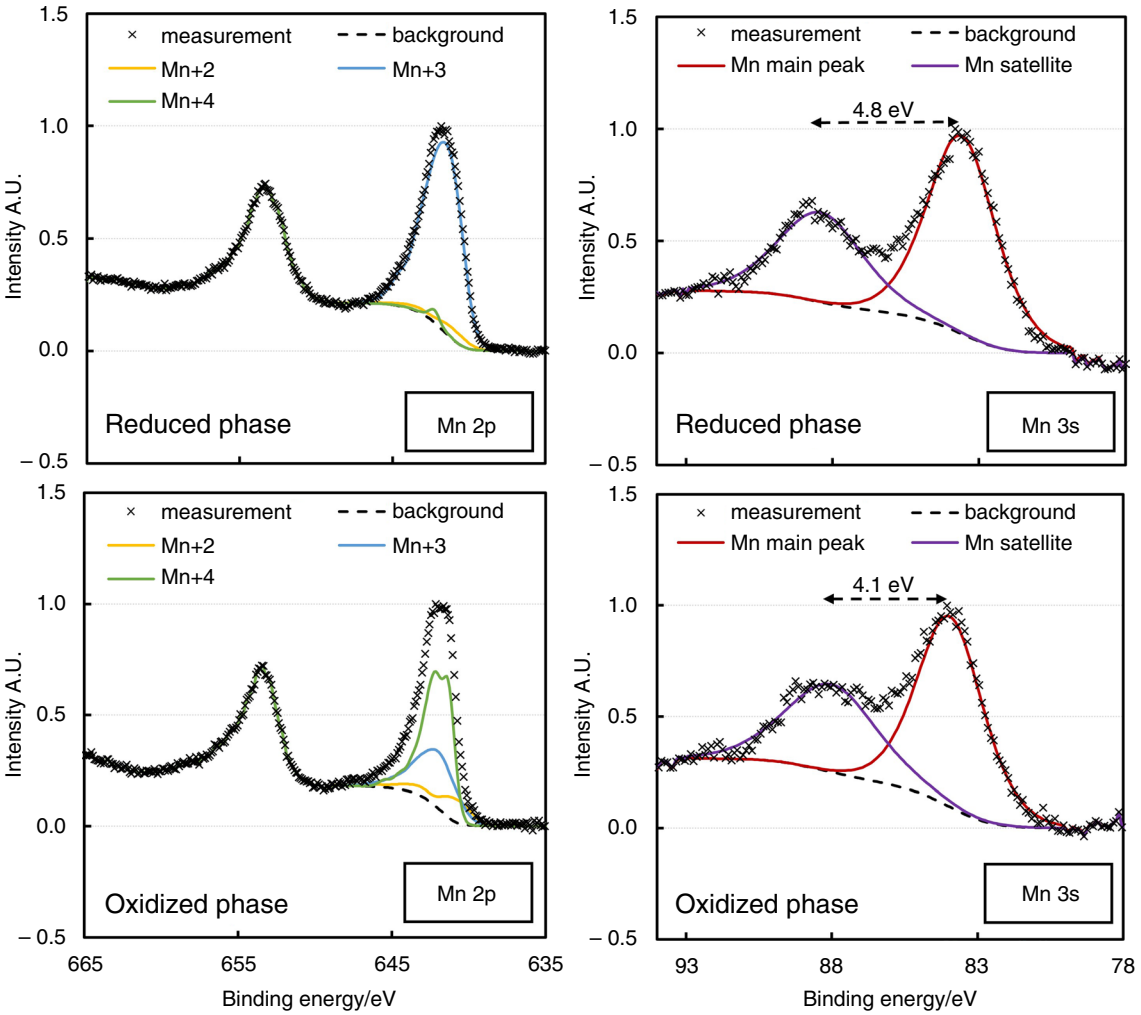

Fig. 8 Mn 2p XPS spectra (left) and Mn 3 s spectra (right) obtained on the reduced (above) and oxidized (below) CAM. The peak fitting components are shown in addition to the acquired data

oxygen capacity is fully charged). If the inlet gas temperature increases to 600 °C or above, it will reduce and the endothermic nature of the reduction reaction brings the gas temperature back to 500 °C (until the material's oxygen capacity is fully depleted).

Further redox experiments between N_2 and air were performed at different temperatures to extract kinetics for the oxidation and reduction of the granulates. As shown in Fig. 6, the oxidized phase is only slightly reduced in N_2 at 420 °C, while in the temperature range from 520 to 560 °C, the capacity is high under atmospheric pressure conditions. (The optimum range will shift to higher temperatures at the elevated pressures associated with IGCC applications.) Three redox cycles between O_2 and N_2 were performed at each temperature—the first one has a larger mass loss than the next two, which are reversible and demonstrates the exact same pattern. What is shown in Fig. 6 is the third cycle (identical to the second cycle). We used the oxidation asymptotes of Fig. 6 (right) to obtain the oxygen stoichiometry $(5+\delta)$ of $Ca_2AlMnO_{5+\delta}$ in 1 atm O_2 at each temperature, and the results are summarized in Fig. 7, which also illustrates the sharp rate of change around 560 °C where the material should be operated for maximum oxygen carrying capacity.

Enthalpies of oxidation of the $Ca_2AlMnO_{5+\delta}$ system

The enthalpies of oxidation obtained from DFT modeling, and TGA, DSC and packed bed experiments are listed in Table 2. In case of DFT calculations, the enthalpy of oxidation is calculated for Eq. 3, *i.e.,* fully oxidized and fully reduced $Ca_2AlMnO_{5.5}$ and Ca_2AlMnO_5 phases. The enthalpy of oxidation calculated by DFT is calculated for ground state (*i.e.,* 0 K). The DSC measurement for enthalpy of oxidation is a direct measurement obtained by the TGA–DSC tests. Gibbs and van't Hoff values for oxidation enthalpies are derived from the packed bed and TGA experiments, respectively. The oxygen partial pressure in equilibrium with the solid bed at each temperature was used to calculate the oxidation enthalpy. In case of Gibbs estimation, gaseous entropy of oxygen gas was included in the calculation as an input and the enthalpy of oxidation was calculated for individual measurements according to Gibbs equation: $\Delta G^\circ = \Delta H^\circ - T\Delta GS^\circ$. In the van't Hoff method, oxygen partial pressure in equilibrium at two different temperatures was used, and the enthalpy of oxidation was calculated according to the van't Hoff equation: $\ln\left(\frac{p_{O_2,2}}{p_{O_2,1}}\right) = \frac{-\Delta H}{R}\left(\frac{1}{T_2} - \frac{1}{T_1}\right)$

Average cationic valences in the oxidized and reduced states at high temperature

The oxidation state of the cations in the Ca_2AlMnO_5 and $Ca_2AlMnO_{5.5}$ structures were first estimated based on the crystal structure by using the bond-valence method developed by Brese & O'Keeffe [39]. The calculations, summarized in Table 3, indicate that the oxidation of Ca_2AlMnO_5 to $Ca_2AlMnO_{5.5}$ does not affect the valence state of aluminum but increases the charge of manganese and calcium.

XPS measurements were performed to evaluate the oxidation state of manganese in the oxidized and reduced CAM samples. Differences in bonds and oxidation state affects the peak shapes of manganese in XPS spectra. Peak fitting of the Mn $2p_{3/2}$ peak using experimental data

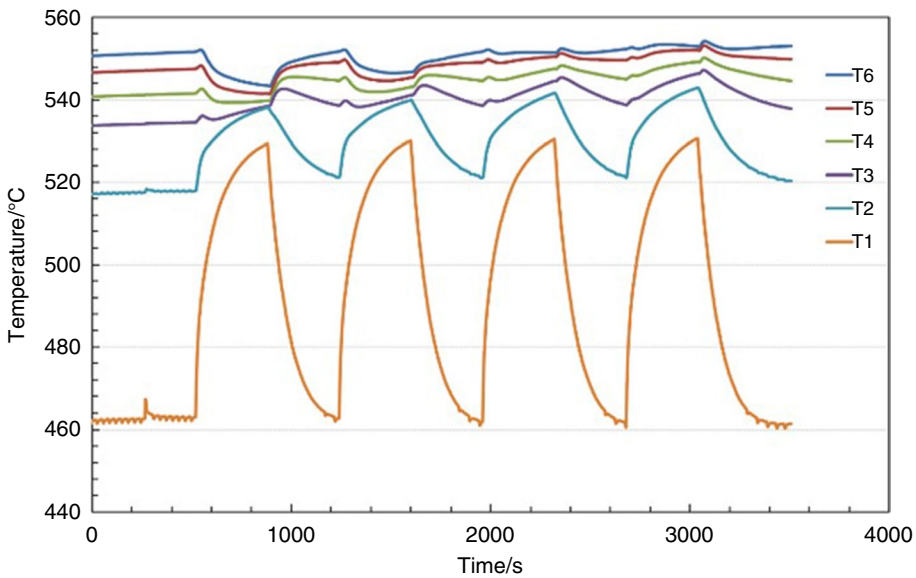

Fig. 9 Temperature evolution in the bed during the oxidation and reduction steps of the TSA. The initial bed temperature is 540 °C. Ar sweep during reduction steps is fed to the bed at 700 °C, and air is charged during the oxidation steps at 400 °C

obtained on pure oxides [40] shows that the peak shape Ca_2AlMnO_5 fits well with the one for Mn_2O_3, while the MnO_2 peak shape dominates for $Ca_2AlMnO_{5.5}$, but still with a notable contribution from Mn_2O_3 as shown in Fig. 8. Average oxidation states for manganese obtained based on these peak fittings are + 3 for the reduced sample and + 3.5 for the oxidized sample (see Table 3). However, it should be kept in mind that the Mn 2*p* peak shape is not only related to the oxidation state but also to the arrangement of the ligands [41]. These values are thus only indicative of the average oxidation of the element. The oxidation state of the first-row transition metals can be assessed too by the separation between the main peak and the satellite of the 3 *s* peak [42]. Peak separations of 4.8 eV and 4.1 eV were determined for the reduced and oxidized samples, respectively (as shown in Fig. 8). These values correspond to an average manganese oxidation state of + 3.4 for Ca_2AlMnO_5 and + 4.3 for $Ca_2AlMnO_{5.5}$.

Packed bed chemical looping oxygen production

Testing fixed bed under cyclic air—argon conditions

Figure 9 shows an example of the temperature evolution inside the packed bed during the oxidation and reduction sequences of the packed bed TSA experiments in this study.

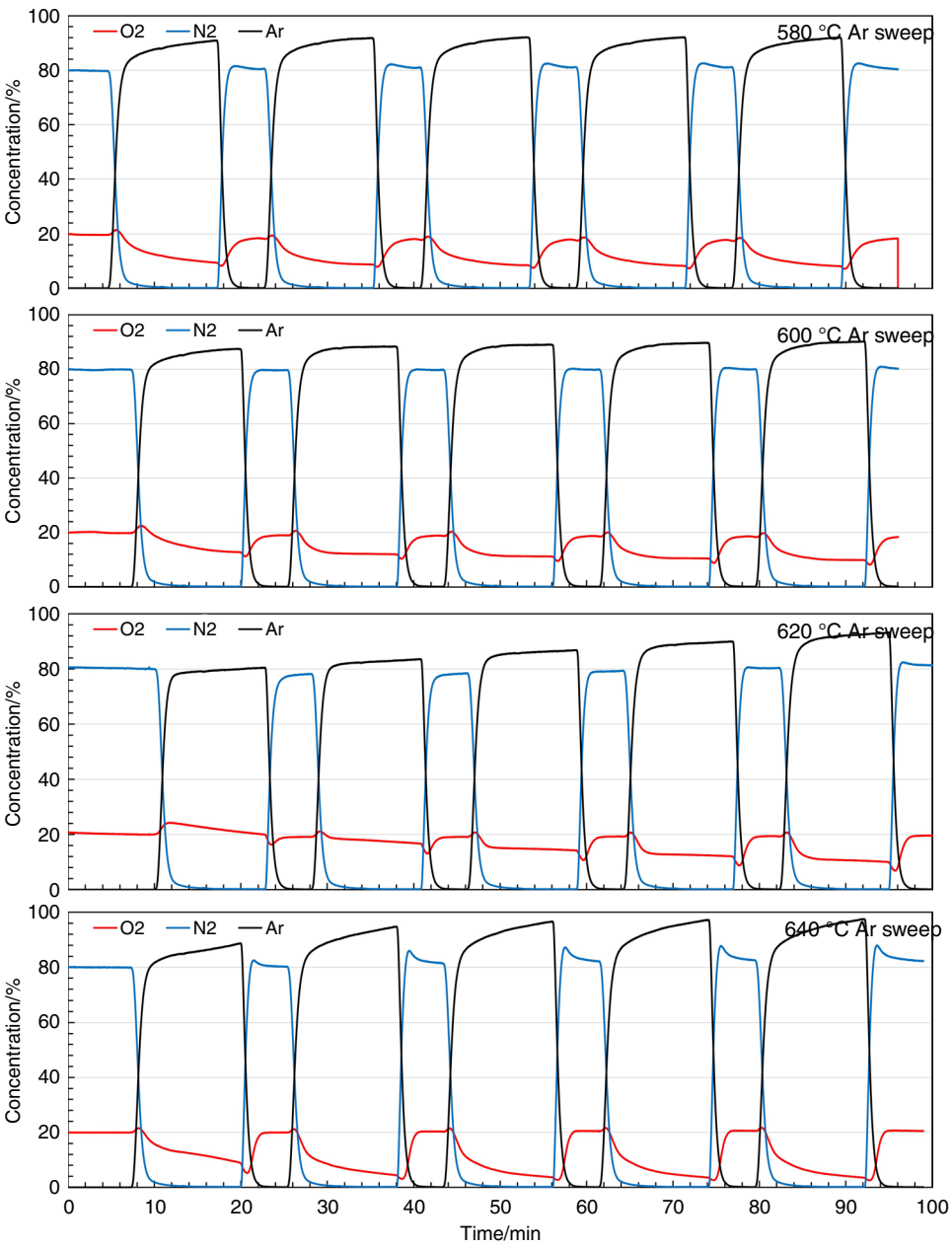

Fig. 10 CLOP into Ar gas under 10 atm pressure at different temperatures, cycling between air 120 L_n h^{-1} (4 min) and Ar 48 L_n h^{-1} (14 min) for several cycles

The thermocouple placements inside the bed and before the bed are illustrated in Fig. 4. The average initial bed temperature in this case (*T*1–*T*5) is 540 °C. Thermocouple *T*6 is embedded in the inert bed beneath the active OCM, and is the very first thermocouple to experience the hot gas that is charged to the reactor from the inline heater. Although *T*6 is embedded in the inert bed (sand with no redox reactivity), *T*6 shows the highest fluctuation in temperature solely due to hot sweep gas (Ar) that is charged to the reactor from the inline heater during the temperature swing experiment (TSA). The temperature of the gas from the inline heater was nominally set to 700 °C during sweep. During reduction, even though hot 700 °C argon is fed to the bed, the bed temperature generally decreases due to the endothermic nature of the reduction reaction (Eq. 1). Conversely, the oxidation of the OCM according to Eq. 2 is exothermic. Therefore, during the second step of the TSA, even though the air fed to the bed is colder than the bed (400 °C), this still results in an increase in the bed temperature during the oxidation.

Packed bed experiments presented in Fig. 10 are performed under isobaric conditions at 10 atm, with gas flow rates of 1600 mL min^{-1} N_2 and 400 mL^{-1} min O_2 during oxidation (total 120 L_n h^{-1}) and 800 mL min^{-1} Ar during reduction (48 L_n h^{-1}). The difference in gas feed temperatures leads to a small TSA effect from the heat carried into the reactor by Ar (70 °C). The oxidizing gas contains 20% O_2 in inert to simulate air, while the inert sweep gas flow rate (Ar) is intentionally lower than the oxidizing gas to increase the percentage of O_2 released during reduction. This semi-optimized condition results in high oxygen production percentage into the inert gas of more than 10%, which is suitable for gasification (where Ar will be substituted by steam or CO_2). Higher oxygen concentrations in the sweep can be achieved if the oxidation step is prolonged, but this could have efficiency consequences because it leads to larger amounts of moderately hot air that must be efficiently integrated into the IGCC process. Another way to improve the reoxidation is by decreasing the temperature of the bed during reoxidation and

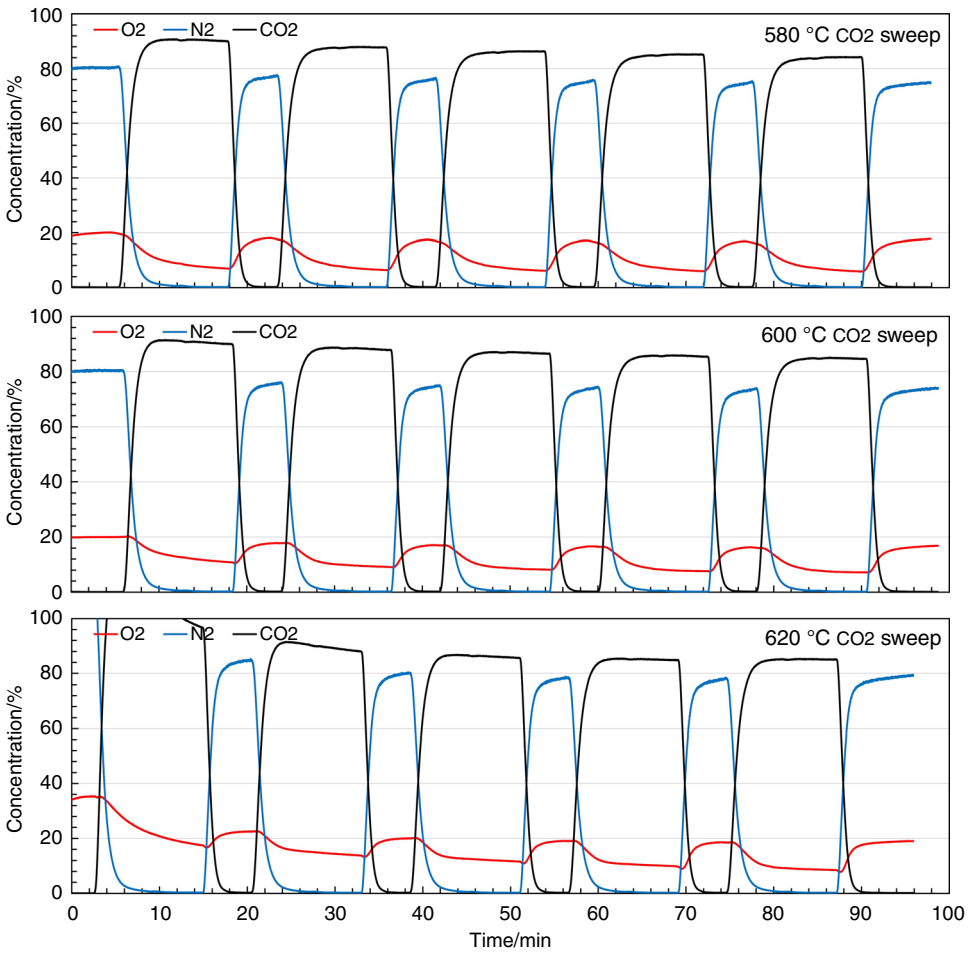

Fig. 11 CLOP into CO_2 gas under 10 atm pressure at different temperatures, cycling between 120 L_n h^{-1} of air (4 min) and 43 L_n h^{-1} of CO_2 (14 min) for several cycles

implementing a proper temperature swing. The bed naturally cools down during the endothermic oxygen release step (reduction); therefore, introduction of hotter sweep will enhance the release of oxygen. In summary, higher temperature for the sweep gas (*i.e.,* returned inert sweep gas of around 600 °C) and lower temperature of air during reoxidation (pressurized air at around 400 °C) should improve the kinetics, as the change in temperature in each step pushes the conditions further away from thermodynamic equilibrium. This mild temperature swing combined with a redox swing (a kind of PSA effect) should create favorable conditions for oxygen transfer into an inert sweep gas, *e.g.,* CO_2.

Figure 10 shows that the highest oxygen release is seen during the first reduction, because the material was heated up in air and therefore fully charged with oxygen before the first step. Still, the oxygen transfer capacity does not decrease steadily after the second cycle until the temperature reaches 620 °C. It is difficult for the OCM to be fully reoxidized in the short oxidation time of the study if the bed temperature exceeds 620 °C, as evident from the TGA experiments as well. The best temperature for the oxygen production is between 600 and 620 °C, where more than 20% oxygen is produced due to the slightly higher temperature of the sweep gas. A larger difference in temperature between streams of oxidation and reduction can increase these numbers further but achieving such a temperature swing may be challenging in a larger reactor.

Testing of fixed bed under cyclic air—CO_2 conditions

The same packed bed experiment with CO_2 as the sweep gas (instead of Ar) is presented in Fig. 11. The results are in line with Ar sweep results, but in this case a slightly lower oxygen percentage in CO_2 is observed. This could be attributed to slightly higher oxygen partial pressure in CO_2 as compared to Ar. Nonetheless, the general trend of increase in

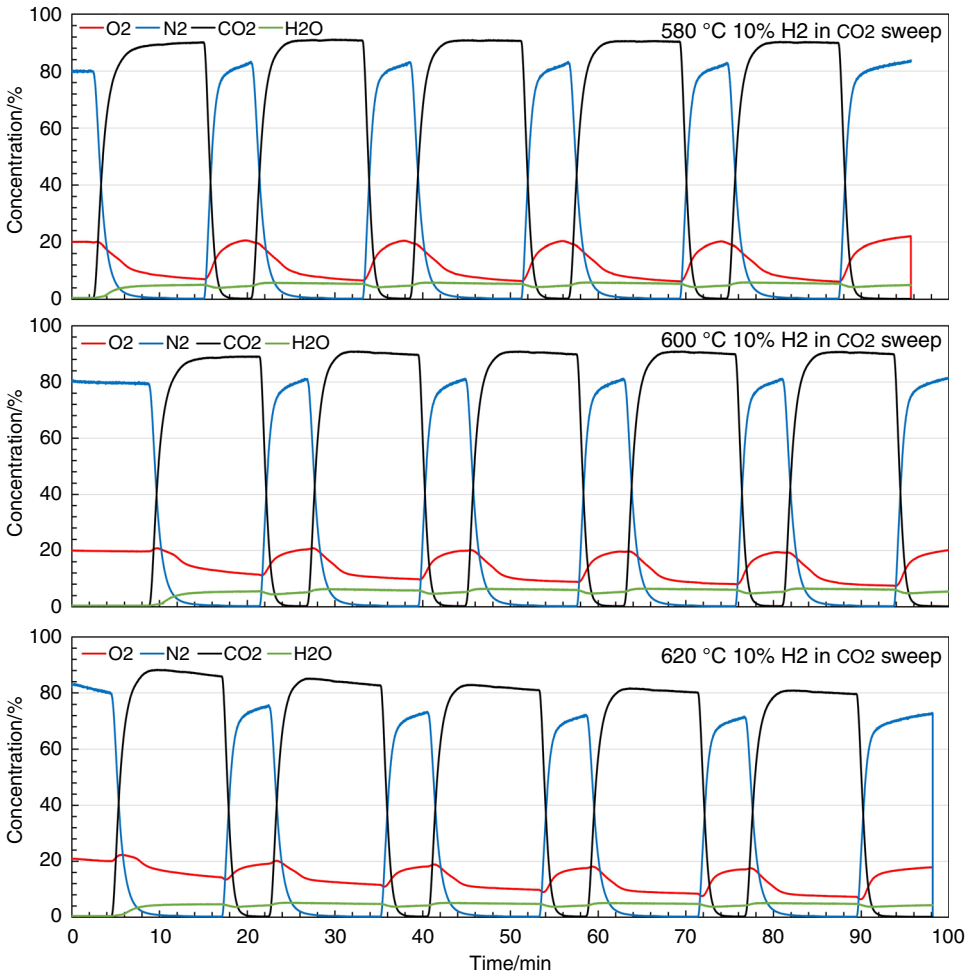

Fig. 12 CLOP into CO_2 gas at 10 atm pressure at different temperatures, cycling between 120 $L_n\ h^{-1}$ of air (4 min), 48 $L_n\ h^{-1}$ of 10% H_2 in CO_2 (2 min) and 43 $L_n\ h^{-1}$ CO_2 (12 min) for several cycles

production up to 620 °C remains unchanged for CO_2 sweep as well.

Testing fixed bed under cyclic air—CO_2/H_2 conditions

Figure 12 shows the packed bed experiment results with CO_2 as the sweep gas, while 10% H_2 was also added to the sweep gas. The idea was that combustion of hydrogen causes a temperature increase of the sweep inside the reactor that may increase the bed temperature during sweep, and therefore increases the oxygen production rate. Such direct fuel combustion would create a much stronger TSA effect than could be achieved by the sensible heat from a hot sweep gas. Unfortunately, the H_2 did not combust with OCM or released O_2 fully and the temperature effect was therefore minimal. In fact, the oxygen release decreased slightly compared to the CO_2 sweep case, which is due to the fact that some of the produced oxygen was consumed by hydrogen. Addition of catalyst to the bed for hydrogen combustion can possibly assist this approach, which will be studied further in the future.

Evaluation of fixed bed tests

In case of Ar sweeping, 10% oxygen was released to the sweep, which corresponds to 1317 mL O_2. The overall oxygen capacity in the fixed bed can be restored during reoxidation because the kinetics for oxidation is faster than reduction (as also shown from the TGA experiments in Fig. 6). However, if 15% oxygen is released to the sweep during the 14 min reduction step, this would correspond to 1980 mL O_2 released from the bed, while the total amount of oxygen supplied to the bed during the 4-min oxidation step is only 1600 mL. This means that the material will not be able to fully recharge during the oxidation step and will gradually deplete from oxygen in a few steps. This is the case of Fig. 13 where the bed is clearly not fully recovered between the cycles since the oxidation step is not fully complete before the gas switches. It should be noted that under a more realistic full cycle condition, the oxidation time will be much longer than the reduction since diluted air is also needed for the CLC part of the system. But in this study, we mainly focused on the redox properties of the material.

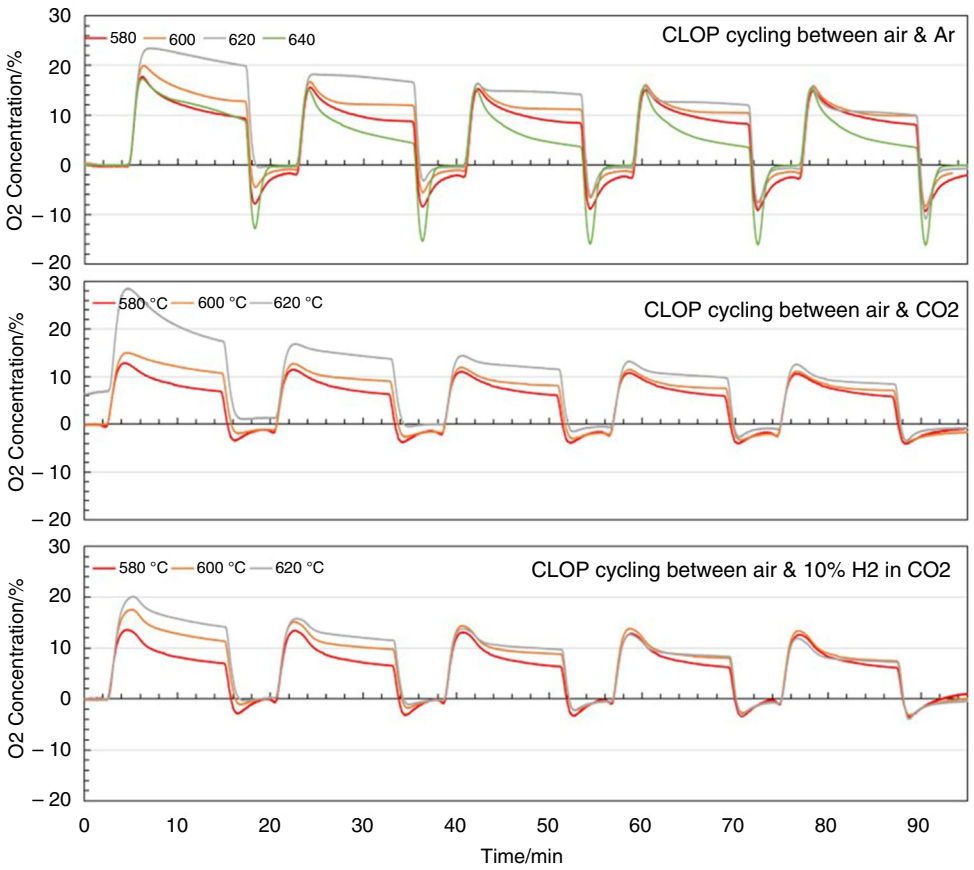

Fig. 13 Oxygen concentration in sweep as a function of flow used during reduction, "negative concentration" is consumed oxygen during bed charging

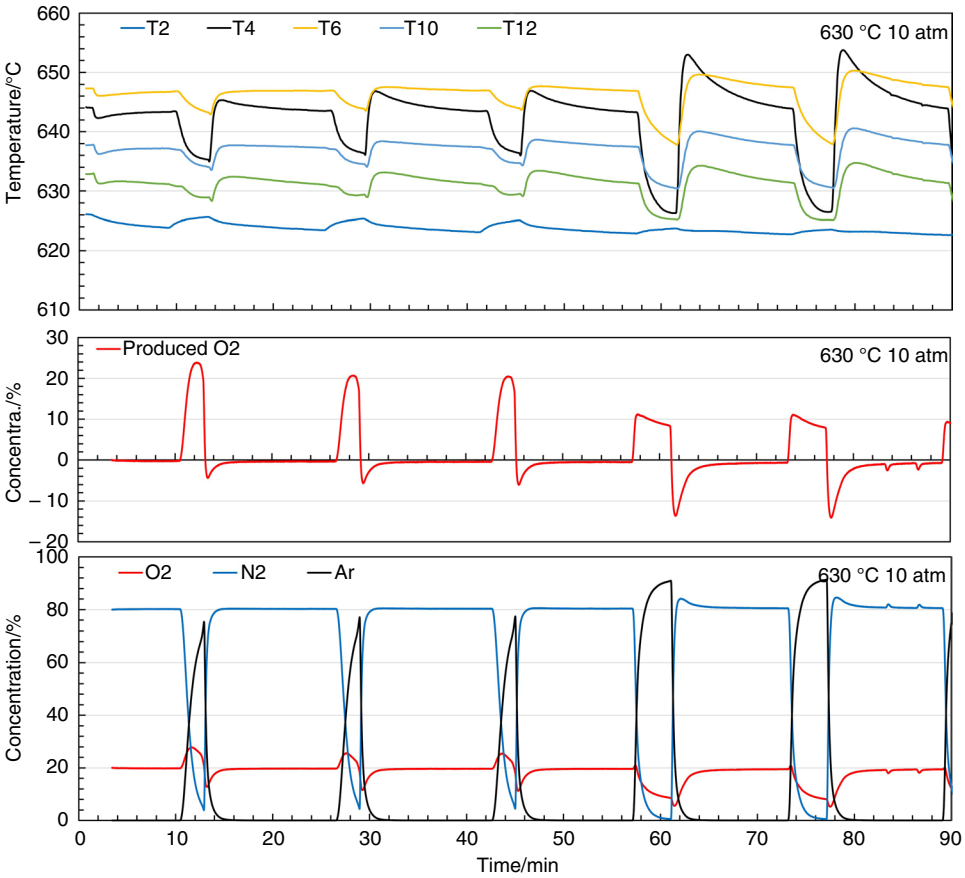

Fig. 14 Cyclic air-inert experiment through the fixed bed reactor for oxygen production into inert 10 atm at 630 ºC for the 5 first cycles. The sweep gas flow rate was 470 mL min^{-1} for the first three cycles and 940 mL min^{-1} for the subsequent two

When using CO_2 as the sweep gas with a slightly lower flow of 720 mL min^{-1}, the amount of oxygen produced becomes even lower compared to Ar sweep at the same temperature (see Figs. 10 and 11). This might be due to CO_2 restricting the release of oxygen by weak absorption or the fact that CO_2 has higher oxygen partial pressure as compared to Ar. Adding H_2 to the CO_2 stream should create a heat wave by combustion, but more efficient release of oxygen that we originally hypothesized did not happen. This was because CAM reduction by H_2 was too deep to be fully reversible and reoxidation lagged, and the bed material was eventually depleted of oxygen after a few cycles.

Packed bed experiments with longer oxidation times

As mentioned earlier (Fig. 1), the integration of CLOP with PBCLC in an IGCC power plant is a promising process configuration for using the CAM material. Different scenarios were simulated for this IGCC configuration, and the main conclusion was that short reduction and long oxidation times gave optimal results. However, in this study a more moderate flow was used to study the effect of flowrate. In these tests, 12 min oxidation in air using 2000 mL^{-1} min (7500 mL^{-1} min when using 2000 mL min^{-1} as sweep) and 4 min reduction using 470 and 940 and 2000 mL^{-1} min was used as sweep. Figure 14 shows the bed temperature profile, and concentrations of gasses during typical air-Ar cycles. In the first 3 cycles, the Ar sweep gas flow rate was 470 mL min^{-1}, while in the following 2 cycles, the Ar sweep gas flowrate was increased to 940 mL min^{-1}. The produced oxygen in the sub-figure is corrected for the air contribution, isolating the oxygen that is produced or consumed by the bed material in %. Thus, the production rate (mol min^{-1}) will be different given the different flows. It is remarkable that the lowest flows produce 20% oxygen, which is the same as used under oxidation. However, for the double sweep flow (940 mL min^{-1}), the concentration is halved, probably due to a combination of kinetic limitations and equilibrium limitations caused by the sharp reduction in temperature.

A small temperature increase can be seen in thermocouple *T*2 when switching to Ar (located right before the bed). This will give a small push on releasing the O_2 since this

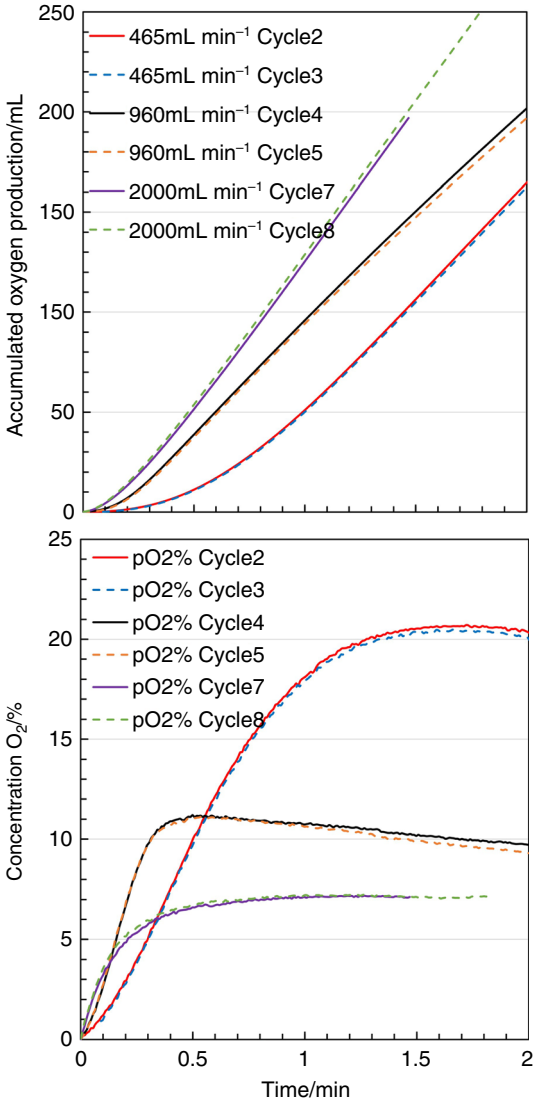

Fig. 15 Evaluation of the oxygen production at 630 ℃

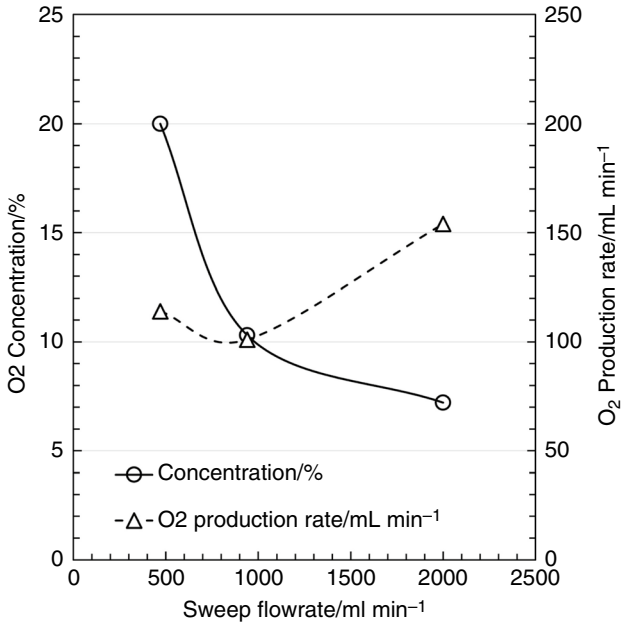

Fig. 16 The average oxygen concentration in the stream and the corresponding O_2 production rate as a function of the sweep flow at 630 ℃

material is very sensitive to temperature (see effect of temperature in Fig. 6). The temperature drops significantly in the beginning of the bed where most O_2 is released into the inert. The temperature decrease is not as severe when being further into the bed because the released O_2 in the inert gas increases the oxygen partial pressure and slows down the oxygen release kinetics.

Figure 15 shows the accumulated oxygen production using different sweep flows. The lowest flowrate results in the highest released oxygen concentrations, as expected, but this will not be the fastest way to remove oxygen from the bed. Higher flowrates lead to higher driving force for release of the oxygen but the concentration of oxygen in inert will be much lower, unless the reactor is extended in length.

Figure 16 summarizes the average oxygen concentration in the sweep and the corresponding O_2 production rate as a function of the sweep flowrate at 630 °C. Doubling the flow nearly halves the concentration of O_2 as expected if diffusion/kinetics is the limiting factor. Increasing the flow further shows that efficient flushing of pores maintains a higher oxygen production than expected from lower flow. This means that surface flushing inside granulates (to keep up the driving force) is of high importance for maximum oxygen production.

As we get closer to the reduction temperature of CAM, the oxygen production rate increases. Figure 17 shows that the maximal concentration is reached close to 640 °C. Internal heating could in principle make it possible to produce high oxygen concentrations but would give more complexity to process operation, unless the internal fuel combustion attempted in Fig. 12 could be successfully achieved. Alternatively, a pressure swing would also increase the oxygen production to some extent.

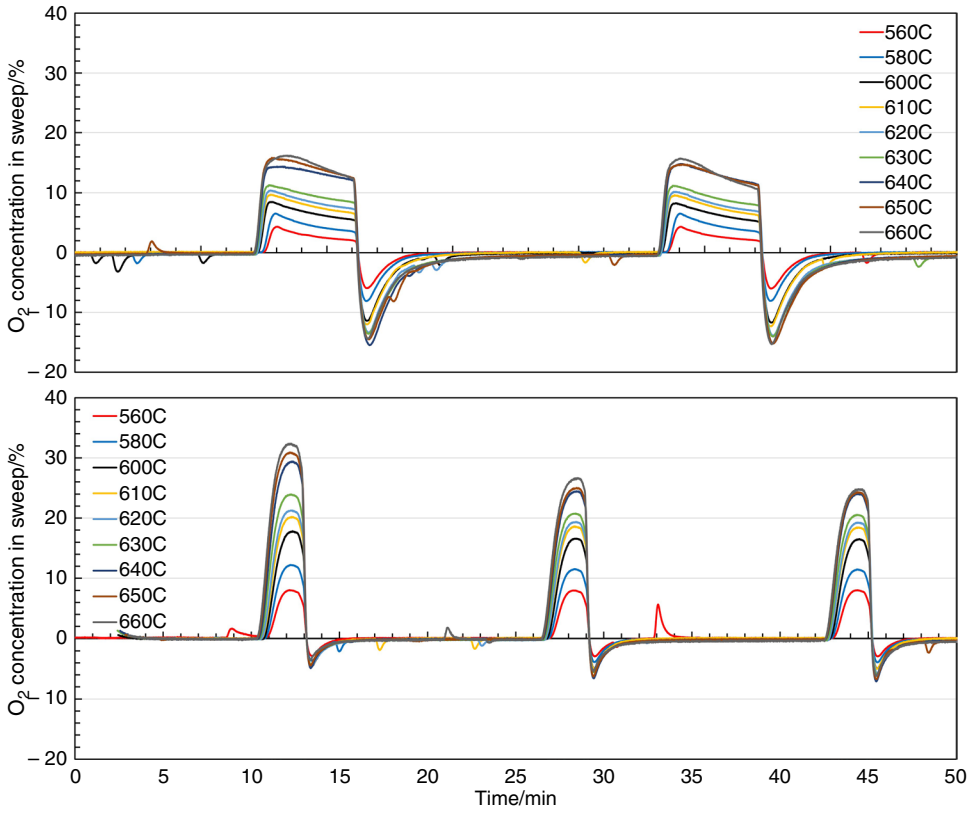

Fig. 17 Top: oxygen concentrations in the sweep gas for cycle 4–5 corrected for air contribution at 10 bar using 970 mL min^{-1} sweep for different temperatures. Bottom: oxygen concentrations in the sweep gas for cycle 1–3 corrected for air contribution at 10 bar using 470 mL min^{-1} sweep for different temperatures

Conclusions

The double-perovskite CAM has demonstrated very interesting and promising properties for oxygen production. Its stability in both oxidizing and reducing conditions results in a long lifetime over many redox cycles. This was verified by post investigation in SEM after testing under different cyclic conditions. The enthalpy of oxidation of $Ca_2AlMnO_{5+\delta}$ was obtained from DFT modeling, equilibrium conditions in thermogravimetric analysis and packed bed experiments, as well as directly from DSC. The enthalpy of oxidation obtained by these techniques range from – 166 to – 196 kJ mol^{-1} O_2. This low enthalpy of oxidation makes the material to release its oxygen content at intermediate temperatures of 400–700 °C to CO_2 or steam, which is suitable for autothermal gasification of solid fuels without nitrogen dilution.

Pressurized reactor tests (10 bar) showed that attractive O_2 concentrations approaching 20% can be achieved during reduction if a long oxidation step can be used to fully oxidize the material beforehand. The large quantity of mildly depleted hot air resulting from such operating conditions needs to be effectively utilized in a downstream process to justify such a configuration, which is possible by integrating the CLOP process with CLC. If such a process integration is not possible, temperature or pressure swings can also increase the concentration of produced O_2, extending the CLOP technology to different applications. Thus, the targeted application must always be kept in mind in future investigations of the CAM material for more efficient oxygen production.

Acknowledgements This study was performed as part of the COMPOSITE project "Combined fixed bed processes for improved energy efficiency and low penalty for CO_2 capture", under the CLIMIT programme; the Grant application no. 239802 funded by the Research Council of Norway. Authors would like to acknowledge CERPOTECH for synthesis and providing the powdered materials used in this study.

Funding Open access funding provided by SINTEF.

References

1. United Nations Framework Convention on Climate Change. The Paris Agreement. 2015. https://unfccc.int/process/the-paris-agreement/the-paris-agreement
2. Energy Technology Perspectives 2017, OCED IEA. International Energy Agency 2018.
3. Ogidiama OV, Abu Zahra M, Shamim T. Techno-economic analysis of a carbon capture chemical looping combustion power plant. J Energy Resour Technol. 2018. https://doi.org/10.1115/1.4040193.
4. Khan MN, Chiesa P, Cloete S, Amini S. Integration of chemical looping combustion for cost-effective CO_2 capture from state-of-the-art natural gas combined cycles. Energy Convers Manag X. 2020;7:100044. https://doi.org/10.1016/j.ecmx.2020.100044.
5. Moghtaderi B. Application of chemical looping concept for air separation at high temperatures. Energy Fuels. 2010;24(1):190–8. https://doi.org/10.1021/ef900553j.
6. Cloete S, Giuffrida A, Romano M, Chiesa P, Pishahang M, Larring Y. Integration of chemical looping oxygen production and chemical looping combustion in integrated gasification combined cycles. Fuel. 2018;220:725–43. https://doi.org/10.1016/j.fuel.2018.02.048.
7. Cloete S, Tobiesen A, Morud J, Romano M, Chiesa P, Giuffrida A, et al. Economic assessment of chemical looping oxygen production and chemical looping combustion in integrated gasification combined cycles. Int J Greenh Gas Control. 2018;78:354–63. https://doi.org/10.1016/j.ijggc.2018.09.008.
8. Peña MA, Fierro JLG. Chemical structures and performance of perovskite oxides. Chem Rev. 2001;101(7):1981–2018. https://doi.org/10.1021/cr980129f.
9. Tofield BC, Scott WR. Oxidative nonstoichiometry in perovskites, an experimental survey; the defect structure of an oxidized lanthanum manganite by powder neutron diffraction. J Solid State Chem. 1974;10(3):183–94. https://doi.org/10.1016/0022-4596(74)90025-5.
10. Anderson MT, Greenwood KB, Taylor GA, Poeppelmeier KR. B-cation arrangements in double perovskites. Prog Solid State Chem. 1993;22(3):197–233. https://doi.org/10.1016/0079-6786(93)90004-B.
11. Saito G, Kunisada Y, Hayami K, Nomura T, Sakaguchi N. Atomic and local electronic structures of $Ca_2AlMnO_{5+\delta}$ as an oxygen storage material. Chem Mater. 2017;29(2):648–55. https://doi.org/10.1021/acs.chemmater.6b04099.
12. Palmer HM, Snedden A, Wright AJ, Greaves C. Crystal structure and magnetic properties of $Ca_2MnAlO_{5.5}$, an n = 3 brownmillerite phase. Chem Mater. 2006;18(5):1130–3. https://doi.org/10.1021/cm052134n.
13. Iseki T, Tamura S, Saito M, Tanabe T, Motohashi T. Tunable oxygen intake/release characteristics of brownmillerite-type $Ca_2AlMnO_{5+\delta}$ involving atomic defect formations. ACS Appl Mater Interfaces. 2021;13(45):53717–24. https://doi.org/10.1021/acsami.1c13534.
14. Motohashi T, Hirano Y, Masubuchi Y, Oshima K, Setoyama T, Kikkawa S. Oxygen storage capability of brownmillerite-type $Ca_2AlMnO_{5+\delta}$ and its application to oxygen enrichment. Chem Mater. 2013;25(3):372–7. https://doi.org/10.1021/cm303156n.
15. Nomura T, Zhu C, Sheng N, Murai R, Akiyama T. Solution combustion synthesis of Brownmillerite-type Ca_2AlMnO_5 as an oxygen storage material. J Alloys Compd. 2015;646:900–5. https://doi.org/10.1016/j.jallcom.2015.06.138.
16. Motohashi T, Kimura M, Inayoshi T, Ueda T, Masubuchi Y, Kikkawa S. Redox characteristics variations in the cation-ordered perovskite oxides BaLnMn2O5+δ (Ln = Y, Gd, Nd, and La) and $Ca_2Al_{1-x}Ga_xMnO_{5+\delta}$ ($0 \le x \le 1$). Dalton Trans. 2015;44(23):10746–52. https://doi.org/10.1039/C4DT03863K.
17. Tian Y, Luongo G, Donat F, Müller CR, Larring Y, Westmoreland PR, et al. Oxygen nonstoichiometry and defect models of brownmillerite-structured $Ca_2MnAlO_{5+\delta}$ for chemical looping air separation. ACS Sustain Chem Eng. 2022;10(31):10393–402. https://doi.org/10.1021/acssuschemeng.2c03485.
18. Tanahashi K, Omura Y, Naya H, Kunisada Y, Sakaguchi N, Kurniawan A, et al. Oxygen separation performance of $Ca_2AlMnO_{5+\delta}$ as an oxygen storage material for high-temperature pressure swing adsorption. ISIJ Int. 2022;62(12):2578–86. https://doi.org/10.2355/isijinternational.ISIJINT-2022-336.
19. Tanahashi K, Omura Y, Naya H, Miyazaki K, Saito G, Kunisada Y, et al. Sr-doped $Ca_2AlMnO_{5+\delta}$ for energy-saving oxygen separation process. ACS Sustain Chem Eng. 2021;9(28):9317–26. https://doi.org/10.1021/acssuschemeng.1c02077.
20. Miura N, Ikeda H, Tsuchida A. $Sr_{1-x}Ca_xFeO_{3-\delta}$ as a new oxygen sorbent for the high-temperature pressure-swing adsorption process. Ind Eng Chem Res. 2016;55(11):3091–6. https://doi.org/10.1021/acs.iecr.5b04579.
21. Wright AJ, Palmer HM, Anderson PA, Greaves C. Structures and magnetic ordering in the brownmillerite phases, Sr_2MnGaO_5 and Ca_2MnAlO_5. J Mater Chem. 2002;12(4):978–82. https://doi.org/10.1039/B109865A.
22. Ling C, Zhang R, Jia H. Quantum chemical design of doped $Ca_2MnAlO_{5+\delta}$ as oxygen storage media. ACS Appl Mater Interfaces. 2015;7(26):14518–27. https://doi.org/10.1021/acsami.5b03729.
23. Sato A, Saito G, Abe K, Kunisada Y, Sakaguchi N, Akiyama T, et al. Rapid oxygen storage and release with Brownmillerite-structured Ca_2AlMnO_5. J Alloys Compd. 2021;851:156817. https://doi.org/10.1016/j.jallcom.2020.156817.
24. Kunisada Y, Saito G, Hayami K, Nomura T, Sakaguchi N. Sr substitution effects on atomic and local electronic structure of $Ca_2AlMnO_{5+\delta}$. Surf Interface Anal. 2019;51(1):65–9. https://doi.org/10.1002/sia.6549.
25. Motohashi T, Ueda T, Masubuchi Y, Kikkawa S. Oxygen intake/release mechanism of double-perovskite type $BaYMn_2O_{5+\delta}$ ($0 \le \delta \le 1$). J Phys Chem C. 2013;117(24):12560–6. https://doi.org/10.1021/jp401965b.
26. Motohashi T, Takahashi T, Kimura M, Masubuchi Y, Kikkawa S, Kubota Y, et al. Remarkable oxygen intake/release of BaYMn2O5+δ viewed from high-temperature crystal structure. J Phys Chem C. 2015;119(5):2356–63. https://doi.org/10.1021/jp511648b.
27. Vøllestad E, Strandbakke R, Tarach M, Catalán-Martínez D, Fontaine M-L, Beeaff D, et al. Mixed proton and electron conducting double perovskite anodes for stable and efficient tubular proton ceramic electrolysers. Nat Mater. 2019;18(7):752–9. https://doi.org/10.1038/s41563-019-0388-2.
28. Carvalho MD, Ferreira LP, Waerenborgh JC, Tsipis E, Lopes AB, Godinho M. Structure and magnetic properties of $Ca_2Fe_{1-x}Mn_xAlO_{5+\delta}$. J Solid State Chem. 2008;181(9):2530–41. https://doi.org/10.1016/j.jssc.2008.06.008.
29. Jain A, Ong SP, Hautier G, Chen W, Richards WD, Dacek S, et al. Commentary: the materials project: a materials genome approach to accelerating materials innovation. APL Mater. 2013;1(1):011002. https://doi.org/10.1063/1.4812323.
30. Perdew JP, Burke K, Ernzerhof M. Generalized gradient approximation made simple. Phys Rev Lett. 1996;77(18):3865–8. https://doi.org/10.1103/PhysRevLett.77.3865.
31. Perdew JP, Burke K, Ernzerhof M. Generalized gradient approximation made simple (vol 77, pg 3865, 1996). Phys Rev Lett. 1997;78(7):1396. https://doi.org/10.1103/PhysRevLett.78.1396.

32. Blochl PE. Projector augmented-wave method. Phys Rev B. 1994;50(24):17953–79. https://doi.org/10.1103/PhysRevB.50.17953.
33. Kresse G, Joubert D. From ultrasoft pseudopotentials to the projector augmented-wave method. Phys Rev B. 1999;59(3):1758–75. https://doi.org/10.1103/PhysRevB.59.1758.
34. Kresse G, Furthmuller J. Efficient iterative schemes for ab initio total-energy calculations using a plane-wave basis set. Phys Rev B. 1996;54(16):11169–86. https://doi.org/10.1103/PhysRevB.54.11169.
35. Wang L, Maxisch T, Ceder G. Oxidation energies of transition metal oxides within the GGA+U framework. Phys Rev B. 2006;73(19):195107. https://doi.org/10.1103/PhysRevB.73.195107.
36. Pishahang M, Mohn CE, Stølen S, Bakken E. DFT-study of the energetics of perovskite-type oxides LaMO3 (M = Sc–Cu). RSC Adv. 2012;2(28):10667–72. https://doi.org/10.1039/C2RA21139D.
37. DeKock RL, Gray HB. Chemical structure and bonding. Sausalito: University Science Books; 1989.
38. Pishahang M, Larring Y, McCann M, Bredesen R. Ca0.9Mn0.5Ti0.5O3−δ: a suitable oxygen carrier material for fixed-bed chemical looping combustion under syngas conditions. Ind Eng Chem Res. 2014;53(26):10549–56. https://doi.org/10.1021/ie500928m.
39. Brese NE, O'Keeffe M. Bond-valence parameters for solids. Acta Crystallogr Sect B. 1991;47(2):192–7. https://doi.org/10.1107/S0108768190011041.
40. Biesinger MC, Payne BP, Grosvenor AP, Lau LWM, Gerson AR, Smart RSC. Resolving surface chemical states in XPS analysis of first row transition metals, oxides and hydroxides: Cr, Mn, Fe, Co and Ni. Appl Surf Sci. 2011;257(7):2717–30. https://doi.org/10.1016/j.apsusc.2010.10.051.
41. Stevie FA, Donley CL. Introduction to x-ray photoelectron spectroscopy. J Vac Sci Technol. 2020;A38(6):063204. https://doi.org/10.1116/6.0000412.
42. Turner NH, Schreifels JA. Surface analysis: X-ray photoelectron spectroscopy and auger electron spectroscopy. Anal Chem. 2000;72(12):99–110. https://doi.org/10.1021/a10000110.